Inorganic Chemistry

Forum Article

pubs.acs.org/IC

Theoretical Spectroscopy and Photodynamics of a Ruthenium Nitrosyl Complex

Leon Freitag and Leticia González*

Institut für theoretische Chemie, Universität Wien, Währinger Straße 17, 1090 Vienna, Austria

ABSTRACT: Photoactive transition-metal nitrosyl complexes are particularly interesting as potential drugs that deliver nitric oxide (NO) upon UV-light irradiation to be used, e.g., in photodynamic therapy. It is well-recognized that quantum-chemical calculations can guide the rational design and synthesis of molecules with specific functions. In this contribution, it is shown how electronic structure calculations and dynamical simulations can provide a unique insight into the photodissociation mechanism of NO. Exemplarily, $[Ru(PaPy_3)(NO)]^{2+}$ is investigated in detail, as a prototype of a particularly promising class of photoactive metal nitrosyl complexes. The ability of time-dependent density functional theory (TD-DFT) to obtain reliable excited-state energies compared with more sophisticated multiconfigurational spin-corrected calculations is evaluated. Moreover, a TD-DFT-based trajectory surface-hopping molecular dynamics study is employed to reveal the details of the radiationless decay of the molecule via internal conversion and intersystem crossing. Calculations show that the ground state of $[Ru(PaPy_3)(NO)]^{2+}$ includes a significant admixture of the $Ru^{III}(NO)^0$ electronic configuration, in contrast to the previously postulated $Ru^{II}(NO)^+$ structure of similar metal nitrosyls. Moreover, the lowest singlet and triplet excited states populate the antibonding metal d → π_{NO}* orbitals, favoring NO dissociation. Molecular dynamics show that intersystem crossing is ultrafast (<10 fs) and dissociation is initiated in less than 50 fs. The competing relaxation to the lowest S_1 singlet state takes place in less than 100 fs and thus competes with NO dissociation, which mostly takes place in the higher-lying excited triplet states. All of these processes are accompanied by bending of the NO ligand, which is not confined to any particular state.

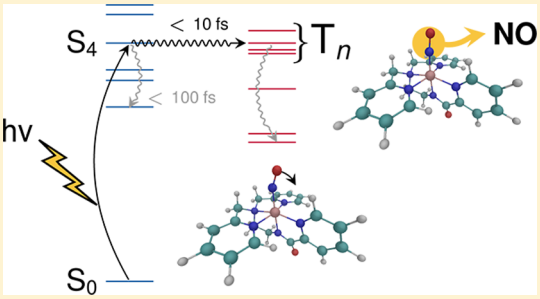

INTRODUCTION

The study of the electronic structure and spectroscopic properties of transition-metal (TM) nitrosyl complexes has long been a subject of interest in inorganic and bioinorganic chemistry. Nitric oxide (NO) plays a role in many biological processes, such as neurotransmission, blood pressure control, or control of tumor growth.[1−3] Following these discoveries, various TM nitrosyl complexes have been investigated as potential carriers able to deliver NO on demand in biological tissues upon illumination, for example to be used in photodynamic therapy (PDT) to treat cancers.[4] Early studies on NO delivery focused on well-known salts, such as sodium nitroprusside $Na_2[Fe(CN)_5(NO)]$, Roussin's salts (NH_4)-$[Fe_4S_3(NO)_7]$ and $Na_2[Fe_2S_2(NO)_4]$)[5,6] or metalloporphyrins, derived from heme.[7,8] However, more recently, in the pursuit to tune the quantum yield and wavelength suitable for the NO photorelease, a number of iron,[9,10] manganese,[11] and ruthenium nitrosyl complexes with other auxiliary ligands[12−16] have been synthesized. In this regard, quite promising is the series of metal nitrosyls $[M(PaPy_3)(NO)]^{2+}$ (M = Fe, Mn, Ru) synthesized by Mascharak and co-workers,[9,11,14] in which the photorelease wavelength is metal-dependent and additionally may be varied by modifying the auxiliary $PaPy_3$ ligand[17] ($PaPy_3$ = *N*,*N*′-bis(2-pyridylmethyl)amine-*N*-ethyl-2-pyridine-2-carboxamide; cf. Scheme 1).

An efficient design of metal−NO carrier complexes can be assisted by electronic structure calculations. In particular, because of its cost-efficiency ratio, density functional theory (DFT) and its time-dependent (TD-DFT) version have become the most popular formalisms to calculate ground- and excited-state properties of TM complexes.[18]

Excited-state TD-DFT studies on TM nitrosyls[19−23] suggest that metal-to-ligand charge-transfer (MLCT) $d_M \rightarrow \pi_{NO}$* states are responsible for their photolability. Yet, different dissociation mechanisms are possible. While in some metal complexes a direct mechanism of NO photorelease via direct population of the $d_M \rightarrow \pi_{NO}$* singlet excited state has been postulated, in others the initial excited state is a MLCT state located in a

Scheme 1

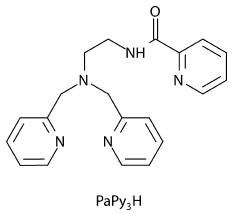

$PaPy_3H$

Special Issue: Insights into Spectroscopy and Reactivity from Electronic Structure Theory

Received: February 4, 2014
Published: April 21, 2014

   dx.doi.org/10.1021/ic500283y | *Inorg. Chem.* 2014, 53, 6415−6426

different ligand (i.e., $d_M \rightarrow \pi_L^*$), and therefore internal conversion is required prior to dissociation in the antibonding $d_M \rightarrow \pi_{NO}^*$ state.[21,22] Moreover, intersystem crossing (ISC) into a $d_M \rightarrow \pi_{NO}^*$ triplet state can also be involved in the NO release.[21−23] These conclusions have been mainly obtained from the theoretical characterization of the absorption spectra obtained from vertical excitation energies and analysis of the Kohn−Sham DFT frontier orbitals of the equilibrium ground state and lowest triplet excited states. Further insight into the dissociation mechanism has also been gained from one-dimensional potential energy scans along the M−NO dissociation coordinate, as in refs 20 and 23.

Beyond stationary quantum-chemical calculations, dynamical simulations could help to reveal further details of the mechanism of NO delivery. In general, a dynamical study allows one to monitor the evolution of the nuclear geometries in time, providing a comprehensive picture of the different states and structures that are visited by the system after light irradiation.[24] In particular, trajectory surface-hopping molecular dynamics[25] is one of the methods most widely employed to simulate nonadiabatic photochemistry beyond the Born−Oppenheimer approximation. It has been employed successfully to explain a large number of ultrafast processes in organic molecules,[26,27] but its application to TM complexes is still in its infancy[28,29] because of the inherent difficulties and computational expenses involved in describing accurately TM complexes with quantum-chemical methods.[30]

Indeed, despite its popularity, the application of TD-DFT to describe the photochemistry of TM complexes is challenging because it requires a balanced description of excited states of very different character.[31] Moreover, the electronic structure of nitrosyl compounds is particularly complicated because of the additional problem of noninnocence of the NO ligand: In metal nitrosyls, NO does not have a clear oxidation state and can exist as NO^+, NO^-, and NO^0.[6,32−36]

Although previous studies on metal nitrosyl complexes[20−22] show satisfactory agreement of the experimental UV−vis absorption spectra with the results calculated with TD-DFT, the most appropriate method to treat these complexes is with multiconfigurational wave-function calculations, such as the complete active space self-consistent-field (CASSCF) method[37] and its second-order perturbation theory version (CASPT2).[38] Indeed, the pioneering work of Pierloot's group in the field of metal nitrosyl complexes[34,39,40] nicely illustrates that CASSCF and CASPT2 are the most adequate methods to describe the complicated electronic structure of these compounds. In general, however, CASSCF/CASPT2 calculations on large TM complexes have remained relatively sparse (see, e.g., refs 30, 31, and 41−43) mainly because of their extensive computational cost. Encouragingly, recent developments in approximation techniques for the two-electron integrals, such as density fitting and Cholesky decomposition,[44] have introduced significant savings of computational time and disk space allowing CASSCF/CASPT2 calculations to be carried out on large TM complexes.[45]

Another important aspect of TM complexes is that, because of the nature of the heavy atom, relativistic effects should be expected. The energies and also the character of the states can be affected by spin−orbit coupling (SOC), influencing their photochemical properties and decay pathways. However, because of the larger computational effort, only a few studies incorporate SOC in the calculation of UV−vis absorption spectra using CASSCF/CASPT2 methods.[46,47] The fact that states of different multiplicity are involved in many photophysical processes of TM complexes is well-known,[48,49] but most studies are limited to analyses of the geometries and orbitals of the lowest singlet and triplet states to explain the reactivity of the TM complex. Calculations including spin dynamics, even if in an approximated way, are exceptional.[29]

In this paper, we push theory in different ways to provide insight into the spectroscopy and reactivity of TM complexes. In particular, we focus on a ruthenium nitrosyl complex, $[Ru(PaPy_3)(NO)]^{2+}$, with the specific aim to learn about the NO dissociation mechanism. Such a study should help to understand the factors that influence the photostability and photodissociation wavelength of these complexes[14] and thus contribute to a rationalization of the drug design for PDT. From a theoretical point of view, this is a contemporary challenge because it implies going beyond the calculation of a UV spectrum for the equilibrium geometry, the optimization of the lowest minimum structures, or the computation of the potential energy curves along one reaction coordinate.[50] Here, we desire to obtain information about relevant geometrical features that are responsible for the reactivity (photodissociation) of metal nitrosyl complexes starting from the bright state. o the best of our knowledge, available studies on this family of complexes have only made use of DFT and TD-DFT and did not account for spin−orbit corrections. Here we shall compute spin-corrected energies and compare the results with the spin-free ones to determine the influence of SOC on the excited-state energies and excitation characters of these complexes. Additionally, we shall assess the applicability of TD-DFT in these compounds by computing the absorption spectra of $[Ru(PaPy_3)(NO)]^{2+}$ with multiconfigurational methods, i.e., with CASPT2. The results will be compared with TD-DFT calculations on metal $PaPy_3$ nitrosyls.[21,22] Finally, and most challenging, time-resolved insight into the NO photorelease mechanism and competing photoprocesses will be obtained by performing a trajectory surface-hopping molecular dynamics study at the TD-DFT level of theory within the singlet- and the triplet-state manifolds. This is, to our knowledge, the first full-dimensional dynamical study on TM nitrosyl complexes.

METHODS AND COMPUTATIONAL DETAILS

Quantum-Chemical Calculations. All DFT and TD-DFT calculations have been performed with the pure BP86[51,52] functional, which has also been employed in the same ruthenium complex and analogous manganese nitrosyl.[21] Moreover, BP86 has the advantage that it allows very fast and efficient computations by employing the resolution-of-identity (RI) approximation for calculating the electronic Coulomb term (RI-J)[53,54] and its multipole-accelerated version (MARI-J).[55] This will be especially important for time savings in the dynamical study, as detailed below. Optimization of the gas-phase equilibrium structure has been carried out using Ahlrichs' def2-SV(P) basis set.[56,57] Additionally, scalar relativistic effects in ruthenium have been accounted for using the quasi-relativistic 28-electron effective core potential (MWB28 ECP).[58] The lowest triplet state has been optimized within the unrestricted DFT formalism. Spin-free electronic excited states have been calculated by means of TD-DFT using the same functional and the def2-TZVPP basis set.[57,59] A total of 30 singlet and 30 triplet excited states have been computed. Solvent effects have been considered using the COSMO solvation model.[60] All of these calculations have been performed with the TURBOMOLE 6.5[61] program package.

Using the BP86 geometry, multiconfigurational spin-free and spin-corrected CASSCF/CASPT2 calculations have been obtained using the MOLCAS 7.8 program package.[62] The active space consisted of 18 electrons in 14 orbitals, including the five Ru 4d orbitals, two pairs of

dx.doi.org/10.1021/ic500283y | Inorg. Chem. 2014, 53, 6415−6426

NO π and π^* orbitals, two σ orbitals that form bonding−antibonding pairs with the Ru $d_{x^2-y^2}$ and d_{z^2} orbitals, respectively, and one $\pi-\pi^*$ pair located at the amide moiety; see Figure 1a. The all-electron ANO-RCC-VTZP basis set[63] has been used for the ruthenium atom and the ANO-RCC-VDZP basis set for other atoms: a CASSCF test calculation with this mixed basis set yielded results almost identical with a calculation with the ANO-RCC-VTZP basis set on all atoms.

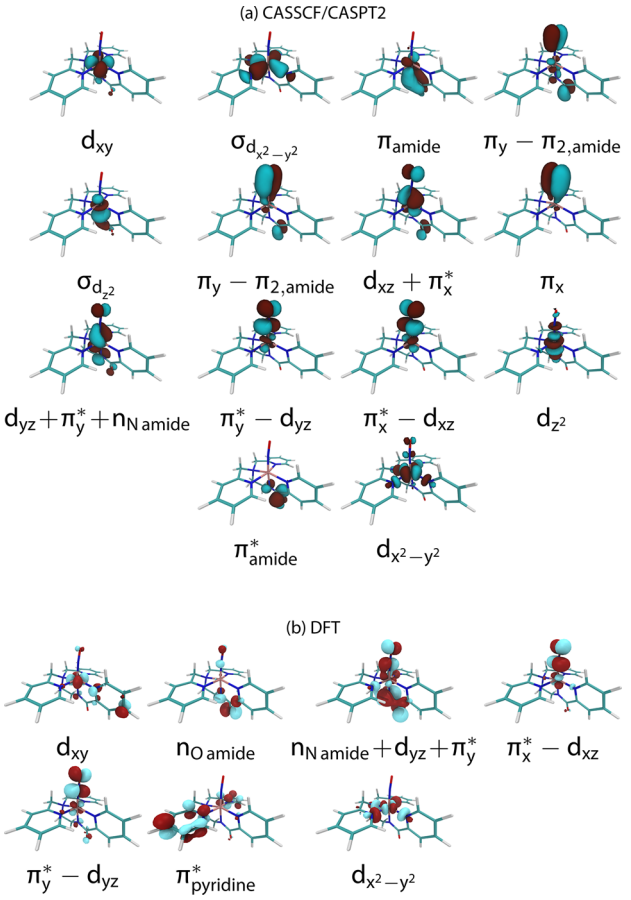

Figure 1. Active orbitals used in CASSCF/CASPT2 calculations (a) and the most important Kohn−Sham DFT orbitals (b). The orbital nomenclature $a \pm b$ indicates that orbital a interacts with b, and the orbital written first has a larger contribution to the resulting molecular orbital than the second one. The sign indicates bonding or antibonding interaction.

For singlet and triplet states, two separate CASSCF calculations have been performed, averaging over 5 singlets and 6 triplets, respectively. The CASPT2 calculations have been done within the multistate approach (MS-CASPT2)[64] using the same number of roots as that in the CASSCF. A level shift[65] of 0.3 a.u. was employed to avoid intruder states. Both CASSCF and MS-CASPT2 calculations employed the Cholesky decomposition-based density fitting approach.[44] The MS-CASPT2 calculations have been performed both in the gas phase and in acetonitrile using the conductor-like polarizable continuum model.[66] The SOC for the MS-CASPT2 wave functions has been calculated with the SO-RASSI method.[67]

Nonadiabatic Molecular Dynamics Simulations. In order to obtain a time-dependent insight of the photodissociation of NO in $[Ru(PaPy_3)(NO)]^{2+}$, nonadiabatic molecular dynamics simulations, where the nuclei move according to classical trajectories that follow Newton's equations in the potential calculated quantum mechanically at every time step, have been performed for the first time in these types of TM complexes. A Wigner distribution for a quantum harmonic oscillator at the ground electronic and vibrational state has been obtained from 400 uncorrelated geometries and velocities. This distribution was created using a geometry optimized with the BP86/def2-SV(P) protocol and a frequency calculation at the same level of theory. From the ensemble of generated geometries, a UV absorption spectrum has been obtained, as explained in ref 68. These calculations also serve to select a number of initial geometries as the initial conditions for the dynamics, according to their oscillator strength and excitation energy. For the nuclear motion, the Velocity Verlet[69] algorithm has been employed with a time step of 0.5 fs. At each time step, on-the-fly energies, gradients, and relevant couplings in the gas phase are calculated.

Ideally, in order to allow internal conversion to compete dynamically with ISC, a code such as SHARC,[70] recently implemented in our group and able to include nonadiabatic coupling and SOC simultaneously, should be used. Because the computation of the CASSCF/CASPT2 electronic properties for TM complexes is currently too time-consuming for on-the-fly calculations, simulations like those performed in smaller organic systems[71] are not possible yet and here we are content with employing TD-DFT. The derivation of TD-DFT-based trajectory surface hopping was given for the first time by Tapavicza et al.,[72] and current TD-DFT molecular dynamics simulations can also include nonadiabatic coupling between ground and excited states as well as between pairs of excited states (see, for instance, refs 73 and 74). Despite the difficulties that TD-DFT experiences to describe regions of near-degeneracy and thus photochemical funnels,[75] remarkable advances are evidenced in the last years in conjunction with nonadiabatic molecular dynamics.[76] However, we are not aware of any code that can currently perform molecular dynamics including on-the-fly TD-DFT SOC; therefore, here a pragmatic and approximate approach has been devised. Two sets of dynamical simulations have been run: one including singlet states and another one starting from triplets from which ISC is highly plausible. Within the singlet manifold, the ground and five lowest excited singlet states were considered and 97 trajectories were started in the S_4 state, according to the oscillator strength and excitation energy of the obtained spectrum. The dynamics of the second set of trajectories in the triplet manifold was executed as follows. The energy levels of the seven lowest triplet states were calculated along the 97 singlet trajectories, and once a triplet state was found close to the current state (<0.01 eV), a new trajectory was spawned with the velocity of the particle in the singlet state but starting in the corresponding triplet state. Only one spawning per trajectory has been performed, resulting in another set of 97 trajectories moving on the triplet-state surfaces. ISC is expected in regions of close degeneracy between singlet and triplet states and nonzero SOC.[47] Therefore, our "manual hopping" is justified as long as SOC is not negligible. This is ensured by looking at the character of the involved singlet and triplet states at the hopping geometries: If the character of the states is different, nonzero SOC is expected. This is an analogy to the El-Sayed rule[77] for organic systems: SOC is large if the transition involves a change of the molecular orbital type. If SOC is nonzero and the potentials are close enough, substantial ISC is expected.[71] As an additional criteria, ISC probabilities have been estimated a posteriori at the hopping geometries with the Landau−Zener model (as was done in refs 78 and 79) using the equation below, where the transition probability P_{ST}^{ISC} from a state S to a state T is given by

$$P_{ST}^{ISC} = 1 - \exp\left(-\frac{\pi}{4}\xi\right); \qquad \xi = \frac{8(H_{ST}^{SO})^2}{\vec{g}_a^{\,ST}\cdot\vec{v}_a}$$

Here, $\vec{g}_a^{\,ST}\cdot\vec{v}_a$ is the dot product of the gradient difference vector for the two states and the velocity vector, obtained at the hopping geometry from the dynamics simulations for each trajectory, and H_{ST}^{SO} is the SOC between the two states. The latter value is taken from the MS-CASPT2 calculations at the equilibrium geometry, as in ref 80. The fact that large probabilities have been found in all cases justifies the manual-hopping procedure. Note that a surface-hopping algorithm based on the Landau−Zener model probabilities instead of using the ad hoc "manual-hopping" procedure could have also been envisaged, given an efficient way to calculate the SOC at each time step would currently exist.

dx.doi.org/10.1021/ic500283y | Inorg. Chem. 2014, 53, 6415−6426

The on-the-fly energy and gradients of the involved singlet or triplet states have been calculated with the BP86 functional in its restricted variant and Ahlrich's def2-SV(P)[56] basis set, within the RI-J and MARI-J approximations, as implemented in the TURBOMOLE 6.5[61] program package. Nonadiabatic coupling is obtained via time-derivative coupling.[81,82]

A locally modified version of the NEWTON-X 1.4 program[83] has been employed to generate the initial conditions, to calculate the UV spectrum, and to simulate the dynamics along 200 fs.

RESULTS AND DISCUSSION

Quantum-Chemical Calculations. *Structural Properties.* The most relevant geometrical parameters of $[Ru(PaPy_3)(NO)]^{2+}$, optimized with DFT for the electronic ground state and lowest singlet (S_1) and triplet (T_1) states are collected in Table 1 (see also Figure 2), together with experimental data.[14]

Table 1. Selected BP86 Bond Lengths and Angles in the $[Ru(PaPy_3)(NO)]^{2+}$ Ground State, T_1 and S_1 Geometry, Compared with the Experimental[14] Structure[a]

	expt	S_0	T_1	S_1
r_{Ru-NO}/Å	1.780	1.807	1.980	1.868
θ_{Ru-N-O}/deg	173.2	172.4	137.5	156.6
$\phi_{O-N_1-Ru-N_2}$/deg			−105.2	0.78
r_{Ru-N_6}/Å	1.997	1.988	1.970	2.041

[a]Distances in angstroms and angles in degrees.

The calculated ground-state geometry is in good agreement with the experimental structure, and because it has already been extensively described in ref 14, we shall only concentrate on the geometrical parameters important for the excited-state transitions.

The most notable change in the geometries upon transition to either T_1 or S_1 is the bend of the nitrosyl ligand: from an almost linear coordination in the ground state (172.4°), the Ru−N−O angle is bent to 156.6° in S_1 or to 137.5° in T_1; see Figure 2. As discussed in the next section, the bend is due to the character of these states, which involve excitation from the $n_{N\ amide} + d_{yz} + \pi_y^*$ orbital (cf. Figure 1; T_1) or the $n_{O\ amide}$ orbital (S_1) to one of the NO π^* antibonding orbitals, i.e., a MLCT and ligand-to-ligand charge-transfer (LLCT) excitation, respectively. Such behavior has already been found in other nitrosyls.[8,34,39] The bending is smaller in S_1 than in T_1 because of less charge transfer (CT) from the metal and more pronounced LLCT character; for the same reason, the Ru−N_6 bond is elongated slightly in S_1 but not in T_1. The bending direction is also different in the excited states (see different dihedral angles $\phi_{O-N_1-Ru-N_2}$): while in S_1 the NO is bent toward N_2, in T_1 it is bent toward N_3.

Ground-State Electronic Structure. While free NO is a radical and contains one unpaired electron in its π^* orbital, both NO^+ and NO^- have closed-shell electronic configurations. In metal complexes, NO can bind to a metal center in different states, such as NO^+, NO^0, or NO^-, making the assignment of oxidation states to NO and the metal center difficult (noninnocency). Enemark and Feltham[84] have established a notation in which such an electronic configuration is represented as $\{M(NO)\}^n$ with n as the total amount of electrons in metal d and NO π^* orbitals. Accordingly, in $[Ru(PaPy_3)(NO)]^{2+}$, the electronic structure is denoted as $\{Ru(NO)\}^6$ and could describe both $Ru^{III}(NO)^0$ and $Ru^{II}(NO)^+$ structures.

On the basis of previous DFT calculations and of the IR stretching frequency of free and bound NO, it has been largely accepted that $\{Ru(NO)\}^6$ nitrosyls are best described as $Ru^{II}(NO)^+$,[36] a structure that corresponds to a d^6 closed-shell occupation of the Ru d orbitals. Our MS-CASPT2 calculations show that the closed-shell d^6 configuration $(d_{xy})^2(d_{xz} + \pi_x^*)^2(d_{yz} + \pi_y^* + n_{N\ amide})^2$ has a weight of 63% and thus the largest contribution to the wave function. Note that weights correspond to configurations built with natural orbitals. As seen in Figure 1, the d_{xz} and d_{yz} metal orbitals interact with the π_{NO}^* orbitals, forming corresponding bonding and antibonding combinations, which indicates strong covalency of the Ru−NO bond. The p_y orbital of the amide nitrogen ($n_{N\ amide}$) also contributes to the $d_{yz} + \pi_y^*$ bonding combination. Similar orbital interactions have been found in the DFT calculations of an analogous manganese complex.[21] Important to understanding the electronic structure of $[Ru(PaPy_3)(NO)]^{2+}$ is that, although the closed-shell configuration has the largest weight, two open-shell configurations, $(d_{xy})^2(d_{xz} + \pi_x^*)^2(d_{yz} + \pi_y^* + n_{N\ amide})^1(d_{yz} - \pi_y^*)^1$ and $(d_{xy})^2(d_{xz} + \pi_x^*)^1(d_{yz} + \pi_y^* + n_{N\ amide})^2(d_{xz} - \pi_x^*)^1$, which represent a back-donation of an electron into the π_{NO}^* orbital and therefore are synonyms of a $Ru^{III}(NO)^0$ structure, have weights of 10 and 8%, respectively [i.e., the total weight of dominant $Ru^{III}(NO)^0$ configurations is 18%]. This means that the ground-state structure of $[Ru(PaPy_3)(NO)]^{2+}$, otherwise accepted as $Ru^{II}(NO)^+$, has a significant contribution of $Ru^{III}(NO)^0$. It is interesting that, despite the fact that DFT cannot account for the admixing of the configurations, it provides good equilibrium geometries, as shown above.

Spin-Free and Spin−Orbit Excited States of $[Ru(PaPy_3)(NO)]^{2+}$. The lowest spin-free singlet and triplet vertical excitation energies, calculated with MS-CASPT2 and TD-

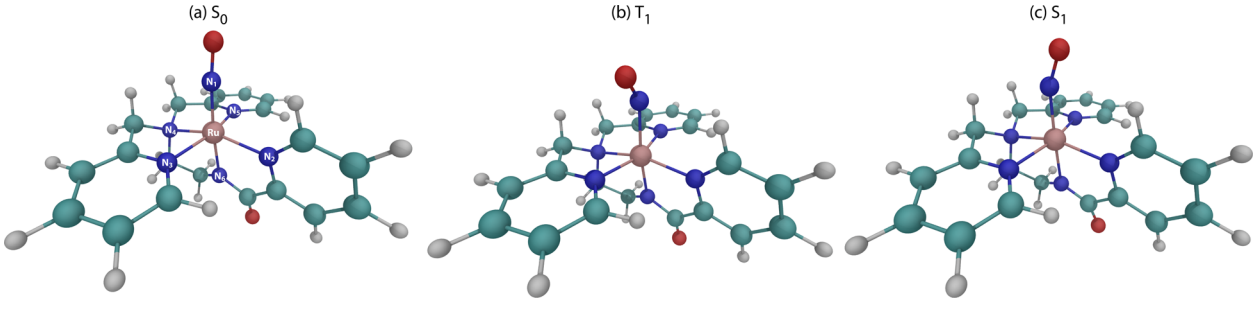

Figure 2. Optimized structure of $[Ru(PaPy_3)(NO)]^{2+}$ in the S_0 (a), T_1 (b), and S_1 (c) states.

dx.doi.org/10.1021/ic500283y | Inorg. Chem. 2014, 53, 6415−6426

Table 2. Spin-Free Lowest Singlet and Triplet Excitations in $[Ru(PaPy_3)(NO)]^{2+}$ Calculated at Different Levels of Theory[a]

method	state	ΔE_{gas}	f_{gas}	ΔE_{solv}	f_{solv}	major contribution	gas c^2 (%)	solv c^2 (%)
CASPT2	T_1	2.46				$d_{yz} + \pi_y^* + n_{N\ amide} \rightarrow \pi_x^* - d_{xz}$	35	
						$d_{xy} \rightarrow \pi_x^* - d_{xz}$	30	
	T_2	2.55				$d_{yz} + \pi_y^* + n_{N\ amide} \rightarrow \pi_y^* - d_{yz}$	53	
	S_1	2.83	0.0003	3.05	0.0001	$d_{xy} \rightarrow \pi_x^* - d_{xz}$	58	63
						$d_{yz} + \pi_y^* + n_{N\ amide} \rightarrow \pi_x^* - d_{xz}$	22	14
	T_3	3.02				$d_{xy} \rightarrow d_{x^2-y^2}$	53	
	T_4	3.09				$d_{xy} \rightarrow \pi_x^* - d_{xz}$	36	
						$d_{yz} + \pi_y^* + n_{N\ amide} \rightarrow \pi_x^* - d_{xz}$	21	
	S_2	3.11	0.0091	3.20	0.0015	$d_{xy} \rightarrow \pi_y^* - d_{yz}$	76	67
	S_3	3.22	0.0003	3.32	0.0004	$d_{yz} + \pi_y^* + n_{N\ amide} \rightarrow \pi_x^* - d_{xz}$	59	54
						$d_{xy} \rightarrow \pi_x^* - d_{xz}$	21	20
	T_5	3.13				$d_{xy} \rightarrow \pi_y^* - d_{yz}$	51	
	S_4	3.50	0.0253	3.67	0.0132	$d_{yz} + \pi_y^* + n_{N\ amide} \rightarrow \pi_y^* - d_{yz}$	48	46
						$d_{xz} + \pi_x^* \rightarrow \pi_x^* - d_{xz}$	31	38
	T_6	3.54				$d_{xz} + \pi_x^* \rightarrow \pi_x^* - d_{xz}$	83	
BP86	T_1	1.66				$n_{N\ amide} + d_{yz} + \pi_y^* \rightarrow \pi_y^* - d_{yz}$	71	
	T_2	1.84				$n_{N\ amide} + d_{yz} + \pi_y^* \rightarrow \pi_x^* - d_{yz}$	77	
	S_1	1.99	0.0000	2.19	0.0002	$n_{N\ amide} + d_{yz} + \pi_y^* \rightarrow \pi_x^* - d_{yz}$	98	80
	T_3	2.05				$n_{O\ amide} \rightarrow \pi_x^* - d_{xz}$	85	
	T_4	2.16				$n_{O\ amide} \rightarrow \pi_y^* - d_{yz}$	87	
	S_2	2.17	0.0002	2.75	0.0062	$n_{O\ amide} \rightarrow \pi_x^* - d_{xz}$	69	31
						$n_{N\ amide} + d_{yz} + \pi_y^* \rightarrow \pi_y^* - d_{yz}$	30	
	S_3	2.24	0.0011	2.73	0.0000	$n_{O\ amide} \rightarrow \pi_y^* - d_{yz}$	77	63
						$d_{xy} \rightarrow \rightarrow \pi_y^* - d_{yz}$		32
	T_5	2.42				$d_{xy} \rightarrow \pi_x^* - d_{xz}$	99	
	T_6	2.50				$d_{xy} \rightarrow \pi_y^* - d_{yz}$	96	
	S_4	2.61	0.0352	2.50	0.0224	$n_{N\ amide} + d_{yz} + \pi_y^* \rightarrow \pi_y^* - d_{yz}$	38	58
						$n_{O\ amide} \rightarrow \pi_x^* - d_{xz}$	–	26
	S_5	2.72	0.0009	2.70	0.0041	$d_{xy} \rightarrow \pi_x^* - d_{xz}$	95	93
	S_6	2.82	0.0083	2.91	0.0352	$d_{xy} \rightarrow \pi_y^* - d_{yz}$	72	31
						$n_{O\ amide} \rightarrow \pi_x^* - d_{xz}$	–	31
	T_7	2.83				$n_{N\ amide} + d_{yz} + \pi_y^* \rightarrow \pi_{pyridine}^*$	71	
	T_8	2.86				$n_{N\ amide} + d_{yz} + \pi_y^* \rightarrow d_{x^2-y^2}$	70	
						$d_{xy} \rightarrow d_{x^2-y^2}$	8	

[a]The excitation energies (ΔE) in electronvolts, oscillator strengths f, main character of the transitions, and corresponding coefficients c^2 are provided. The "gas" subscript stands for properties calculated in the gas phase and the "solv" subscript for properties calculated in acetonitrile.

DFT/BP86, are collected in Table 2. Values for singlet excitations are reported in the gas phase and acetonitrile.

According to the MS-CASPT2 calculations, the lowest four singlet states are mainly MLCT transitions from the ruthenium center to antibonding Ru–NO ($\pi_x^* - d_{xz}$ and $\pi_y^* - d_{yz}$) orbitals. Two states are bright. The brightest state corresponds to S_4, is predicted at 3.50 eV, and is characterized by a $n_{N\ amide} + d_{yz} + \pi_y^* \rightarrow \pi_y^* - d_{yz}$ transition, i.e., by a transition from a Ru–NO bonding orbital to the corresponding antibonding orbital with some admixing of a LLCT transition from the $n_{N\ amide}$ orbital; see the orbitals in Figure 1a. The second brightest state is S_2; it is located at 3.11 eV and corresponds to a pure MLCT transition, $d_{xy} \rightarrow \pi_y^* - d_{yz}$. This transition would be forbidden in an octahedral ligand field but here becomes partially allowed because of deviations from the octahedral coordination geometry. The S_1 and S_3 states are much weaker in intensity

dx.doi.org/10.1021/ic500283y | Inorg. Chem. 2014, 53, 6415–6426

and play little role in the absorption spectrum. The inclusion of acetonitrile in the calculation is reflected in a solvatochromic blue shift of 0.09−0.22 eV but does not alter the order of the singlet states. Noticeable is that the intensity of the S_2 state decreases in solution, so that the spectrum in acetonitrile is dominated by the bright S_4 state, which is now predicted at 3.67 eV.

The MS-CASPT2 results show a good agreement with the experimental spectrum, reproduced in Figure 3. The spectrum,

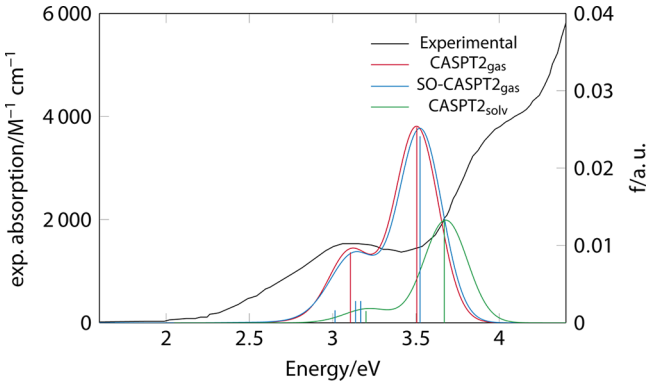

Figure 3. Convoluted spectra obtained with MS-CASPT2 in the gas phase (gas), including spin−orbit (SO) corrections, and in solution (solv). The experimental absorption spectrum of $[Ru(PaPy_3)(NO)]^{2+}$ is also depicted, reproduced from ref 21 (solid line, left *y* axis).

recorded in acetonitrile,[21] shows a broad band around ca. 3.8 eV and a less intense one at ca. 3.2 eV. The low-energy peak can then be assigned to the weaker MLCT $d_{xy} \rightarrow \pi_y^* - d_{yz}$ transition ($S_0 \rightarrow S_2$), and the second, more intense shoulder is due to the brighter MLCT (and partially LLCT) $n_{N\ amide} + d_{yz} + \pi_y^* \rightarrow \pi_y^* - d_{yz}$ transition (S_4). The latter transition is underestimated by MS-CASPT2 by about 0.2 eV. The convoluted absorption spectra obtained from the theoretical MS-CASPT2 calculations are also shown in Figure 3 for comparison.

The gas-phase TD-DFT/BP86 results agree qualitatively with those obtained by MS-CASPT2; see Table 2. The brightest state is also S_4, although underestimated by ca. 0.9 eV, with respect to the gas-phase MS-CASPT2 value. The character of the transition is the same, although the mixing of the orbitals differs slightly. The second bright state, found as S_2 with MS-CASPT2, is S_6 with BP86. This state is predicted at 2.82 eV and thus underestimated by ca. 0.3 eV from the MS-CASPT2 value. Because the errors in both excitations are different, the state order predicted by BP86 is different from that obtained with MS-CASPT2, and thus the assignment of the lowest experimental band is missing at the BP86 level of theory. Regarding the other singlet states, BP86 also finds a LLCT state (S_3) at 2.24 eV, which is not present at the MS-CASPT2 level of theory because the corresponding $n_{O\ amide}$ orbital is not contained in the active space. Because the oscillator strength of this state is comparatively small, it is not expected to contribute to the spectrum. Inclusion of the solvent model in TD-DFT calculations has a more dramatic effect on the excited-state energies and properties than that in MS-CASPT2: the states mix more with each other, which is reflected in less systematic solvent shifts and oscillator strength changes.

BP86 calculations of higher-lying excited states show a high density of bright MLCT $d \rightarrow \pi_{pyridine}^*$ and LLCT $\pi_{pyridine}^* \rightarrow \pi_{pyridine}^*$ transitions (cf. Figure 1b), which could contribute to the rising higher-energy band above 4 eV; see Figure 3. These states are not relevant for photodissociation of NO, and therefore they will not be further discussed.

Despite the fact that BP86 has been widely used for TM complexes,[85] it is well-known that non-range-separated functionals (such as BP86) do not optimally describe CT excitations.[86] In $[Ru(PaPy_3)(NO)]^{2+}$, BP86 systematically underestimates the absorption energies with respect to both the experimental and MS-CASPT2 values. However, the magnitude of the error seems to be different depending on the CT character of the transition, which leads to different orders of the states and could lead to a misinterpretation of the spectrum. Excitations involving the $n_{N\ amide}$ orbitals with partial LLCT character (such as S_1 and S_4) are underestimated by almost 1 eV (compare the BP86 and gas-phase MS-CASPT2 values in Table 2), while transitions involving the metal d_{xy} orbital (such as the S_6 at BP86) have a much smaller error. This difference can be explained by the larger spatial separation of the n_{Namide} and π_{NO}^* orbital compared to the metal d_{xy} orbital; see Figure 1b. The more accentuated the CT character, the more problematic is the description of the state. The LLCT S_3 state at 2.24 eV has a spatial separation of the frontier orbitals similar to that of the excitation involving the n_{Namide} orbital and is therefore expected to be red-shifted within by BP86 by a similar amount of energy.

Despite the errors, the qualitative description of the lowest singlet excited states with BP86 seems to be largely in accordance with the MS-CASPT2 results and supports the fact that the MLCT excitations into Ru−NO antibonding orbitals, which are highly relevant for NO photodissociation, lie at the lower end of the absorption spectrum and do not mix with other states.

The triplet states are, in principle, not important for the peak assignment in the absorption spectrum, but they are relevant for the photodissociation mechanism of NO. Just like their singlet counterparts, the lowest triplet excited states are also predominantly of MLCT character; see Table 2. An exception is the T_3 state, which at MS-CASPT2 is a ligand-field or $d \rightarrow d$ transition. This $d \rightarrow d$ transition shows by far the largest SOC to the ground state of 1013 cm^{-1}, which is reflected in the absorption spectrum: the first bright state in the spin−orbit-coupled MS-CASPT2 calculation (labeled SO-CASPT2 in Figure 3) has a T_3 weight of approximately 76%. Its bright character is not attributed to the large ground-state SOC but rather to large SOC to the bright S_2 state. Figure 4 shows the most important SOC between the singlets and triplets, calculated at the MS-CASPT2 level of theory. As can be seen, the S_2 state has strong SOC with T_4 and T_5, which results in a splitting of the bright S_2 peak in the spin-free spectrum into three different transitions with large S_2 contributions. This splitting, however, is rather small, for the resulting three transitions are at most 0.15 eV apart. The brightest state, S_4, is only slightly influenced by SOC. It mixes with the closest-lying T_6 state, but the SOC is comparatively small (37 cm^{-1}), and thus it blue-shifts by only 0.02 eV. The small SOC is compatible with the El-Sayed rule[77] in the sense that the S_4 and T_6 state characters are very similar, and therefore a small coupling is expected. For comparison, SOC between other states can reach values of up to 460 cm^{-1}.

Despite SOC, the convoluted SO-CASPT2 spectrum is very similar to that obtained spin-free; see Figure 3. In other TM complexes, such as rhenium and iridium complexes, for

dx.doi.org/10.1021/ic500283y | Inorg. Chem. 2014, 53, 6415−6426

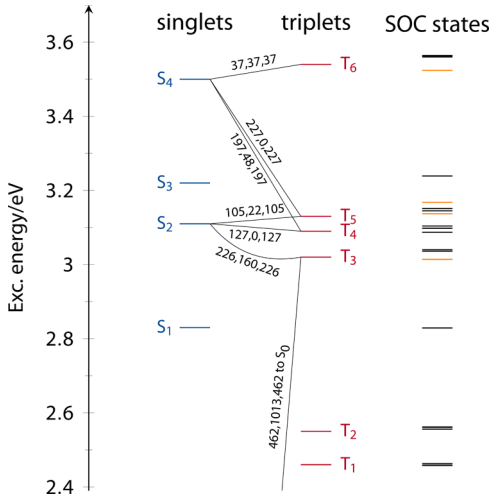

Figure 4. Important SOC (in cm^{-1}) calculated at the CASPT2 level of theory: bright spin−orbit states are shown in orange.

example, the influence of SOC has been shown to be larger.[46] Despite the fact that spin-free energies are sufficient to calculate the absorption spectrum, the presence of large SOC between singlet and triplet states undermines the importance of the triplet states for dissociation.

As in the case of the singlet states, TD-DFT/BP86 systematically underestimates MLCT triplet excitation energies by 0.62−0.89 eV, but this error is systematic and quantitatively similar for a given class of excitations.

NO Photodissociation Mechanism. According to the spin-free static calculations, the most optically active state in the near-UV region is the S_4 state. This is predominantly an MLCT state that populates the Ru−NO antibonding orbital, with an admixture of LLCT character from the amido nitrogen coordinated trans to NO. Between this state and the ground state, there is a manifold of other MLCT excited states (singlets and triplets) populating Ru−NO antibonding orbitals, which could easily be accessed by internal conversion (singlets) or ISC (triplets) and could all potentially lead to NO dissociation. The introduction of SOC does not change the absorption spectrum qualitatively; it only increases the density of states (cf. Figure 4).

This picture is compatible with the "direct" mechanism postulated earlier[21,22] in which NO dissociation is prompted by the direct population of a $d_M \rightarrow \pi_{NO}^*$ MLCT singlet excited state, with the addenda that the dissociation may occur also from the analogous triplet states after ISC. As such, it is then in contrast to the "indirect" mechanism postulated in the analogous $[Mn(PaPy_3)(NO)]^{2+}$ complex,[21] where internal conversion to the $d_M \rightarrow \pi_{NO}^*$ MLCT is required prior to dissociation.

In order to obtain more details about the actual NO photodissociation mechanism and the features that accompany this process, a gas-phase surface-hopping molecular dynamics study has been carried out. Dynamical simulations have been done at the TD-DFT/BP86/def2-SV(P) level of theory, which provides an overall qualitative picture of the spectroscopy of $[Ru(PaPy_3)(NO)]^{2+}$, despite the fact that the energies of the MLCT states are systematically underestimated with respect to the MS-CASPT2 ones.

From single-point vertical excitation calculations at the 400 initial conditions generated from the Wigner distribution, a total spectrum restricted to the lowest four excited singlet states has been calculated. This spectrum is obtained as the sum of the four contributions coming from the S_1−S_4 excited states. The spectra arising from each state, as well as the total absorption spectrum, are shown in Figure 5. One can see that

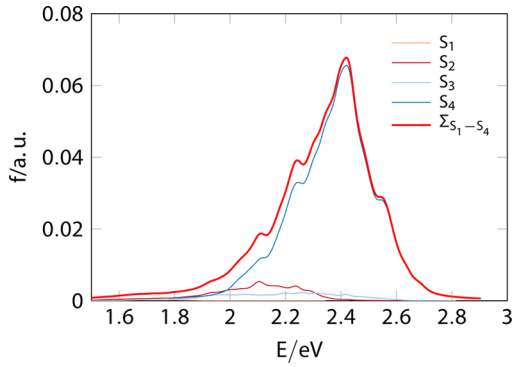

Figure 5. Absorption spectra of $[Ru(PaPy_3)(NO)]^{2+}$ calculated from excitation energies for a Wigner distribution of geometries. The total spectrum ($\sum_{S_1-S_4}$), as well as those obtained from each individual excitation, is depicted. The full-width at half-maximum employed to convolute the spectra was 0.05 eV.

the total UV spectrum almost entirely consists of the S_4 contribution, indicating that nonequilibrium geometries obtained from the zero-point-energy quantum distribution of the molecule also are excited primarily to the S_4 state. Therefore, all trajectories have been prepared in S_4 as the initial state, covering the full energy band. Recall that the obtained band corresponds to the experimental shoulder extending from ca. 3.5 to 4.2 eV.

The possibility of ISC from S_4 has been approximated with a Landau−Zener model, as explained in the Methods and Computational Details section. The obtained singlet−triplet transition probabilities should be considered upper limits, but with up to 90%, they point to a very efficient ISC. The most probable transitions are those from S_4 to the $d_{xy} \rightarrow \pi_{x-d_{xz}}^*$ and $d_{xy} \rightarrow \pi_{y-d_{yz}}^*$ MLCT T_5 and T_6 states (T_4 and T_5 in MS-CASPT2; recall Table 2) and to T_7. The calculated SOC values for $S_4 \rightarrow T_4$ (T_5 in BP86) and $S_4 \rightarrow T_5$ (T_6 in BP86) are 197 and 227 cm^{-1}, respectively (cf. Figure 4). For the $S_4 \rightarrow T_7$ transition, no probability could be calculated because the state is not present at the MS-CASPT2 level of theory and thus no SOC is available; however, here SOC is also expected to be large based on the El-Sayed propensity rule. Figure 6 depicts the time distribution at which ISC was obtained during the first 20 fs. From the 97 trajectories, 46% undergo ISC in the first 2 fs, 85% within the first 10 fs, and over 90% in the first 20 fs. These numbers should also be considered an upper bound because only one trajectory was spawned per singlet and back-transfer from the triplets is not allowed. However, it is clear that a large fraction of the initial S_4 population can undergo an ISC to a MLCT $d_{xy} \rightarrow \pi_{x-d_{xz}}^*$ or $d_{xy} \rightarrow \pi_{y-d_{yz}}^*$ triplet state already in the first 10 fs. This ultrafast ISC is in line with experiments done in other TM complexes, where extremely short time scales for ISC have been measured (even below 30 fs).[48]

Along the singlet and triplet trajectories, the most important changes in the geometry are stretching of the Ru−NO bond and bending of the NO ligand. The time evolution of these two geometrical parameters is shown in Figure 7. Most trajectories

dx.doi.org/10.1021/ic500283y | Inorg. Chem. 2014, 53, 6415−6426

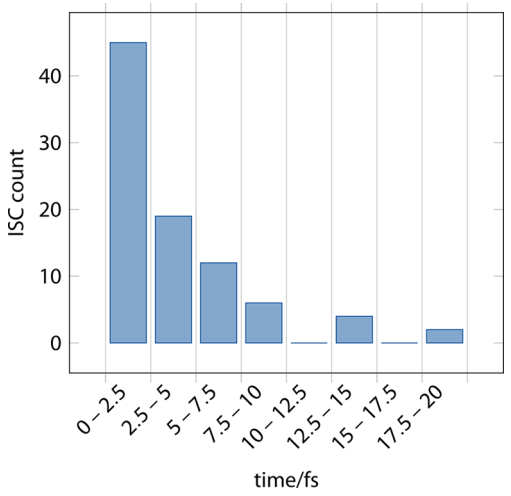

Figure 6. Number of ISC during the first 20 fs.

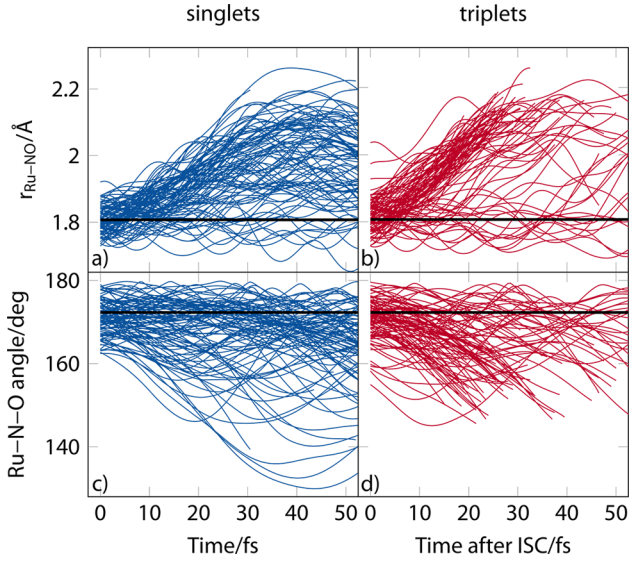

Figure 7. Time evolution of Ru–NO distances (a and b) and Ru–N–O angles (c and d) for each trajectory in singlet (a and c) and triplet (b and d) states in the first 50 fs. The solid black lines in each plot indicate the values at equilibrium.

clearly show an increase in the Ru–NO distance (Figure 7a,b) in the first 30 fs. Other Ru–N bonds oscillate randomly and do not increase their average value during the simulation time, indicating that they are not relevant for NO photorelease. NO dissociation appears to be slightly faster for the triplet trajectories than for the singlet ones. Unfortunately, a large number of triplet trajectories crash shortly after the Ru–N distance reaches 2.1–2.2 Å because at these extended Ru–N bond distances the S_0 and T_1 states become degenerate, a situation that DFT cannot handle. Therefore, Figure 7 is only plotted until 50 fs, a time for which we consider the results to be meaningful. Despite the limitations of TD-DFT, we interpret this Ru–NO bond extension as the beginning of NO dissociation and not just as a Ru–NO vibration because of its concerted nature.

The time scale of 20–30 fs, at which dissociation is initiated, is not enough for most trajectories to relax to the lowest excited state; i.e., NO readily dissociates in the triplet excited states. Note that singlet and triplet excitations within TD-DFT could be described with different accuracy, especially in geometries differing significantly from the equilibrium one, affecting the predicted dissociation times. However, because here we are only able to describe the beginning of the dissociation process, which takes place in an extremely short time scale, we expect this effect to hardly affect the reported time scales. Most of the triplet trajectories show NO dissociation in the $d_{xy} \rightarrow \pi_x^* - d_{xz}$, $d_{xy} \rightarrow \pi_y^* - d_{yz}$ MLCT states or sometimes in the $n_{N\ amide} + d_{yz} + \pi_y^* \rightarrow \pi_{y-d_{yz}}^*$ state, either directly or involving one or two internal conversions between the triplet states.

The bond stretching observed in the singlet trajectories (Figure 7a) is also ascribed to NO dissociation. In this case, propagation of the singlet states does not suffer from the S_0–T_1 degeneracy problem because the T_1 state is not present in the calculation, but analysis is equally restricted to the first 50 fs because DFT cannot properly dissociate.[87,88]

Indeed, a CASSCF rigid scan of the Ru–NO distance while keeping all other coordinates frozen at the equilibrium geometry shows the dissociative nature of the singlet excited states (Figure 8a) and the increase of the ground-state weight

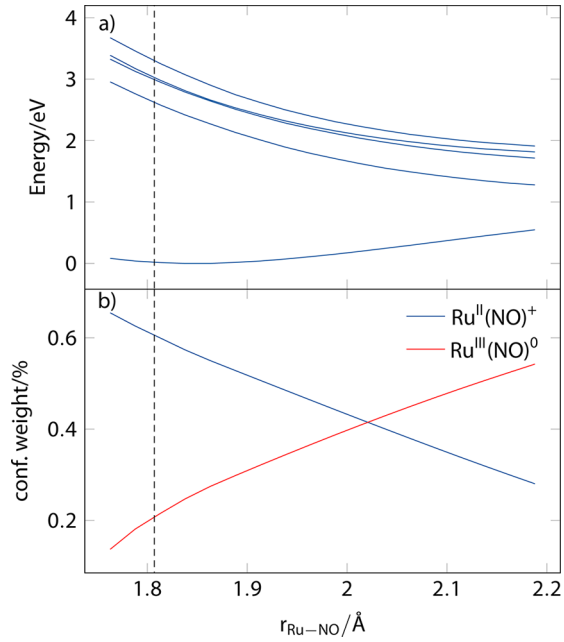

Figure 8. (a) Energies of the ground and the first four singlet excited states from the Ru–NO distance scan with CASSCF. All other geometry parameters were kept at their equilibrium geometry values. (b) Configuration weight of the principal $Ru^{II}(NO)^+$ and $Ru^{III}(NO)^0$ configurations in the ground state. The dashed black line indicates the equilibrium Ru–NO distance at the BP86 geometry.

of the open-shell $Ru^{III}(NO)^0$ configuration built with natural orbitals (Figure 8b). At around 2 Å, both $Ru^{III}(NO)^0$ and $Ru^{II}(NO)^+$ electronic configurations reach 50% and, accordingly, the ground state cannot be described reliably by DFT anymore.

The singlet trajectories show efficient internal conversion: within the first 50 fs, over 30% of the trajectories decay from S_4 to S_1 (Figure 9a). Note that the present TD-DFT implementation in NEWTON-X does not support hopping from S_1 to S_0, so trajectories can only be trapped in the S_1 state. The target S_1 state is also a MLCT or LLCT state, populating the NO π^* orbital either from the $n_{N\ amide} + d_{yz}$, the $n_{O\ amide}$, or a mixture of both, and from our Ru–NO analysis, population in

dx.doi.org/10.1021/ic500283y | Inorg. Chem. 2014, 53, 6415–6426

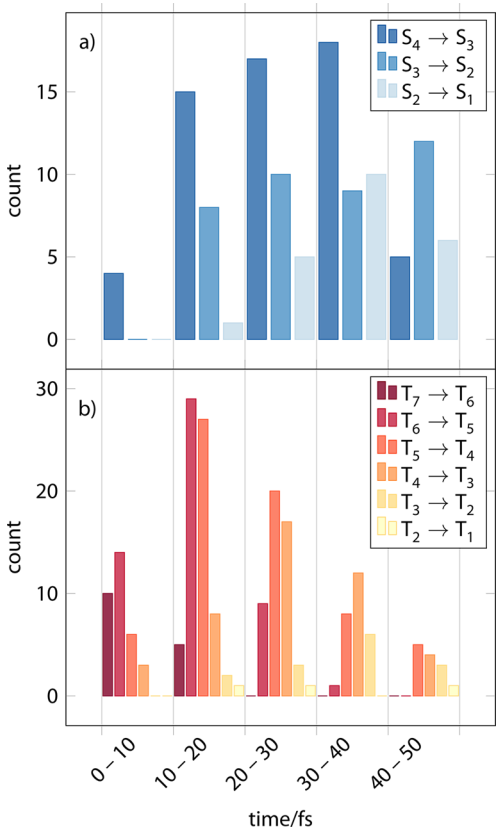

Figure 9. Frequency of internal conversions to the lowest excited states for the singlet (a) and triplet (b) trajectories in the first 50 fs.

this state does not prompt dissociation, in agreement with the fact that an equilibrium structure for the S_1 state can be optimized (see above).

Another key geometrical change present in most of the trajectories is bending of the NO ligand (Figure 7c,d). It is precisely the bending of NO that brings the S_0, S_1, and T_1 states close together, with the concomitant problem for TD-DFT terminating the calculation. During the first 20 fs, $[Ru(PaPy_3)(NO)]^{2+}$ evolves from mostly a linear structure to angles of ca. 150°. This bending is consistent with the optimized geometry of the S_1 and T_1 structures, which are also bent, and with the character of the lowest MLCT states because they represent excitation into a NO π^* antibonding orbital, i.e., a $Ru^{III}(NO)^0$ configuration, which is favored upon NO bending. NO bending is also found along the concerted Ru–NO bond elongation in triplets, but it is not a necessary requirement for dissociation.

In theoretical photochemistry, it is an usual goal to characterize conical intersections, which are the structures that facilitate an ultrafast funnel between two electronic states, i.e., radiationless internal conversion. As seen in Figure 9, the number of internal conversions among the singlet and among the triplet states, respectively, is relatively large in the first 50 fs. Already during the first 10 fs, $S_4 \rightarrow S_3$ internal conversion is taking place. After another 10 fs, the conical intersection mediating the $S_3 \rightarrow S_2$ transition is operative and gradually the nonadiabatic $S_2 \rightarrow S_1$ transition is also efficient. Internal conversion among the triplets (Figure 9b) is even more efficient because the distribution of sequential hops is rather generalized. Figure 10 shows a global mechanism of the deactivation of $[Ru(PaPy_3)(NO)]^{2+}$, summarizing all time scales and processes predicted by the present simulations.

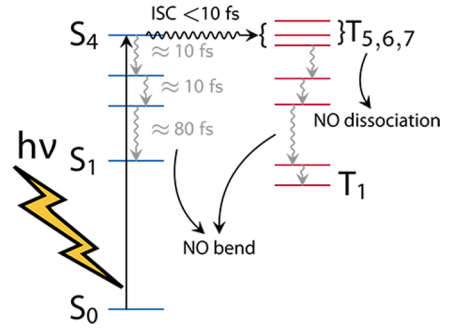

Figure 10. Schematic deactivation mechanism of $[Ru(PaPy_3)(NO)]^{2+}$.

In order to obtain insight into the geometrical changes that characterize the conical intersections among singlet and triplet states, respectively, a convoluted spectral distribution of selected parameters (Ru–NO bond length, Ru–N–O bond angle, and other Ru–N bonds) at the different hopping geometries is shown in Figure 11, together with the same convoluted distribution for the initial geometries generated with a Wigner distribution. The comparison between the different distributions indicates the temporal evolution of these parameters. The first thing to notice is that already the geometries belonging to the Wigner distributions include a broad spectrum of values. Then, it is obvious that the Ru–N

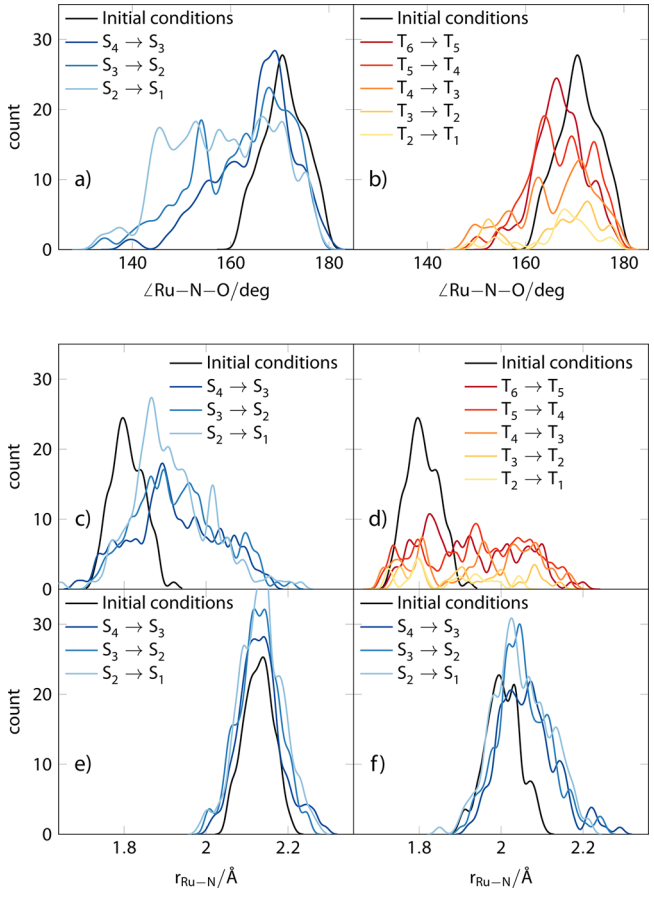

Figure 11. Gaussian convolution of the distribution of various geometrical parameters in singlet and triplet hopping geometries: (a and b) Ru–NO angles in singlet and triplet geometries; (c and d) Ru–NO distances in singlet and triplet geometries, (e and f) Ru–N_5 and Ru–N_6 distances in singlet hopping geometries.

dx.doi.org/10.1021/ic500283y | Inorg. Chem. 2014, 53, 6415–6426

bonds, different from NO (Figure 11e,f), show little change in the dynamics; that is, the peaks of the distributions do not show significant deviations at any of the hopping geometries, making it difficult to assign a particular value characteristic of a conical intersection.

In contrast, the distributions of the Ru−NO bond lengths and Ru−N−O angles for the singlets (Figure 11a,c) and triplets (Figure 11b,d) are significantly different from the initial values at all hopping geometries. The Ru−NO distance at the Franck−Condon geometry is 1.807 Å, which corresponds to the peak of the Wigner distribution. As can be seen (Figure 11c), after excitation to S_4 and internal conversion to S_3, the Ru−NO stretches on average to 1.9 Å. The next internal conversion from $S_3 \rightarrow S_2$ is accompanied by a broader distribution of Ru−NO bond distances, centered around 1.9 and 2.0 Å, while $S_2 \rightarrow S_1$ relaxation is characterized by an averaged distance smaller than 1.9 Å, indicating that the majority of the relaxation to S_1 occurs at a bond distance close to the equilibrium one. In the triplet states (Figure 11d), the distribution of Ru−NO bond lengths is significantly broader than that for the singlet states at any of the hopping geometries, making it difficult to assign a conical intersection with a particular value. While one still can locate a slight maximum for $T_6 \rightarrow T_5$ hop, at approximately 1.82 Å, still fairly close to the equilibrium geometry, this maximum is smeared out as the trajectories proceed nonadiabatically to lower triplet states, which is consistent with the dissociating behavior of some of the trajectories.

For the Ru−N−O bond angle dependence (Figure 11a,b), also broad distributions are obtained. Yet, the cascade of both singlet and triplet conical intersections is accompanied of bending of the NO fragment. The initial $S_4 \rightarrow S_3$ transition is so fast (10 fs; see Figure 9a) that the molecule does not have time to bend; therefore, a large peak is found at almost the same angle as that in the Franck−Condon geometry. Hops to the lower states show lower angles, which means that most of the bending occurs in the S_3 and S_2 states. In the triplet states, the change in the angle is faster, as we can see in the decrease of the maxima toward lower angles as the trajectories proceed to T_1 (although there always remains a small maximum close to the equilibrium values).

CONCLUSIONS

In this paper, we investigated the electronic structure of $[Ru(PaPy_3)(NO)]^{2+}$ ground and excited states using spin-corrected MS-CASPT2 calculations. Moreover, we obtained insight into the NO photodissociation mechanism using TD-DFT-based trajectory surface-hopping molecular dynamics.

The ground state of $[Ru(PaPy_3)(NO)]^{2+}$ is a singlet and shows linear NO coordination, in line with many other TM nitrosyls. In contrast, the excited states show significant bending of the NO ligand, which is attributed to CT from either the metal or the carboxamido group of PaPy to NO. Although this complex is usually considered to be of mainly $Ru^{II}(NO)^+$ character, our MS-CASPT2 calculations show a significant contribution of $Ru^{III}(NO)^0$ configurations to its ground state.

Excited-state MS-CASPT2 calculations reproduce well the UV−vis absorption spectra and show that the lowest singlet and the majority of lowest triplet excited states are MLCT excitations in the antibonding metal $d \rightarrow \pi_{NO}^*$ orbitals. Spin-corrected calculations show large SOC of the triplet states up to 1013 cm^{-1} with the ground state and up to 460 cm^{-1} between singlet and triplet excited states. The calculated SOC between singlets and triplets with similar character is an order of magnitude smaller, which is consistent with the El-Sayed rules, extrapolated to TM complexes. Although the large SOC values are not reflected quantitatively in the absorption spectrum, they can facilitate ultrafast ISC, which is calculated to happen to a significant amount already in the first 10 fs.

Within the first 50 fs, the trajectories propagating in both the singlet or triplet states show Ru−NO bond elongation, a fact that can be ascribed to Ru−NO dissociation. This dissociation is more accentuated in the $d_{xy} \rightarrow \pi_x^* - d_{xz}$ and $d_{xy} \rightarrow \pi_y^* - d_{yz}$ triplet MLCT states, which are populated after the ISC from the bright $d_{yz} + \pi_y^* + n_{N\ amide} \rightarrow \pi_y^* - d_{yz}$ MLCT state. A similar pathway is found in the singlet trajectories; in this case, however, radiationless internal conversion from S_4 to S_1 competes with NO dissociation. Unfortunately, full decay to the ground state cannot be observed within our TD-DFT dynamical calculations; therefore, absolute decay times are not provided, but both dissociation and internal conversion take place in less than 100 fs. All of these processes are accompanied by bending of the NO ligand, which is not confined to any particular state.

Besides stretching of the Ru−NO bond and bending of the NO ligand, no other characteristic geometrical feature is found to be relevant for NO photodissociation. Likewise, no particular geometry could be assigned to any of the different conical intersections mediating internal conversion within the singlet or triplet states, respectively. The hopping geometries show a very broad distribution of geometrical parameters, with a pattern similar to that obtained initially due to the zero-point energy.

In general, we found that the fully atomistic description of dynamical processes involving nonadiabatic effects, different multiplicities, and bond breaking is extremely challenging for the standard formulation of TD-DFT, as employed here in the on-the-fly calculations. However, and despite its limitations, surface-hopping nonadiabatic simulations are very useful to providing key insight into the photodynamics of this class of molecules. Clearly, the development of methods that are able to describe the photodynamics of TM complexes is an exciting and rewarding area of research, which we will surely see flourish in the coming years.

AUTHOR INFORMATION

Corresponding Author

*E-mail: leticia.gonzalez@univie.ac.at.

Notes

The authors declare no competing financial interest.

ACKNOWLEDGMENTS

We thank the University of Vienna for financial support and the COST Action CM1202 for inspiring a number of theoretical problems on ruthenium complexes. The authors also thank Vladimir Arion, as well as Sebastian Mai and Philipp Marquetand for enlightening discussions on nitrosyl complexes and dynamics, respectively. All of the calculations were performed in the HP computers of the Theoretical Chemistry Group at the University of Vienna.

REFERENCES

(1) (a) Culotta, E.; Koshland, D. E. *Science* **1992**, *258*, 1862−1865. (b) Fang, F. C. *Nitric Oxide and Infection*; Springer: Berlin, 1999. (c) Ignarro, L. J. *Nitric Oxide: Biology and Pathobiology*; Academic Press: New York, 2000.

(2) Rose, M. J.; Mascharak, P. K. *Curr. Opin. Chem. Biol.* **2008**, *12*, 238−244.
(3) Tfouni, E.; Truzzi, D. R.; Tavares, A.; Gomes, A. J.; Figueiredo, L. E.; Franco, D. W. *Nitric Oxide* **2012**, *26*, 38−53.
(4) Detty, M. R.; Gibson, S. L.; Wagner, S. J. *J. Med. Chem.* **2004**, *47*, 3897−3915.
(5) (a) Bourassa, J.; Lee, B.; Bernard, S.; Schoonover, J.; Ford, P. C. *Inorg. Chem.* **1999**, *38*, 2947−2952. (b) Conrado, C. L.; Bourassa, J. L.; Egler, C.; Wecksler, S.; Ford, P. C. *Inorg. Chem.* **2003**, *42*, 2288−2293.
(6) Jaworska, M.; Stasicka, Z. *J. Mol. Struct.* **2006**, *785*, 68−75.
(7) (a) Ford, P.; Bourassa, J.; Miranda, K.; Lee, B.; Lorkovic, I.; Boggs, S.; Kudo, S.; Laverman, L. *Coord. Chem. Rev.* **1998**, *171*, 185−202. (b) Hoshino, M.; Laverman, L.; Ford, P. C. *Coord. Chem. Rev.* **1999**, *187*, 75−102.
(8) Ford, P. C.; Lorkovic, I. M. *Chem. Rev.* **2002**, *102*, 993−1018.
(9) Patra, A. K.; Afshar, R.; Olmstead, M. M.; Mascharak, P. K. *Angew. Chem., Int. Ed.* **2002**, *41*, 2512−2515.
(10) Patra, A. K.; Rowland, J. M.; Marlin, D. S.; Bill, E.; Olmstead, M. M.; Mascharak, P. K. *Angew. Chem., Int. Ed.* **2003**, *42*, 6812−6823.
(11) Eroy-Reveles, A. A.; Leung, Y.; Beavers, C. M.; Olmstead, M. M.; Mascharak, P. K. *J. Am. Chem. Soc.* **2008**, *130*, 4447−4458.
(12) Works, C. F.; Ford, P. C. *J. Am. Chem. Soc.* **2000**, *122*, 7592−7593.
(13) Works, C. F.; Jocher, C. J.; Bart, G. D.; Bu, X.; Ford, P. C. *Inorg. Chem.* **2002**, *41*, 3728−3739.
(14) Patra, A. K.; Mascharak, P. K. *Inorg. Chem.* **2003**, *42*, 7363−7365.
(15) (a) Rose, M. J.; Olmstead, M. M.; Mascharak, P. K. *J. Am. Chem. Soc.* **2007**, *129*, 5342−5343. (b) Rose, M. J.; Mascharak, P. K. *Chem. Commun.* **2008**, 3933−3935. (c) Fry, N. L.; Mascharak, P. K. *Acc. Chem. Res.* **2011**, *44*, 289−298.
(16) Bohlender, C.; Wolfram, M.; Goerls, H.; Imhof, W.; Menzel, R.; Baumgaertel, A.; Schubert, U. S.; Mueller, U.; Frigge, M.; Schnabelrauch, M.; Wyrwa, R.; Schiller, A. *J. Mater. Chem.* **2012**, *22*, 8785−8792.
(17) Rose, M. J.; Olmstead, M. M.; Mascharak, P. K. *Polyhedron* **2007**, *26*, 4713−4718.
(18) Cramer, C. J.; Truhlar, D. G. *Phys. Chem. Chem. Phys.* **2009**, *11*, 10757−10816.
(19) Tfouni, E.; Krieger, M.; McGarvey, B. R.; Franco, D. W. *Coord. Chem. Rev.* **2003**, *236*, 57−69.
(20) De Candia, A. G.; Marcolongo, J. P.; Etchenique, R.; Slep, L. D. *Inorg. Chem.* **2010**, *49*, 6925−6930.
(21) Merkle, A. C.; Fry, N. L.; Mascharak, P. K.; Lehnert, N. *Inorg. Chem.* **2011**, *50*, 12192−12203.
(22) Fry, N. L.; Mascharak, P. K. *Dalton Trans.* **2012**, *41*, 4726−4735.
(23) Zheng, W.; Wu, S.; Zhao, S.; Geng, Y.; Jin, J.; Su, Z.; Fu, Q. *Inorg. Chem.* **2012**, *51*, 3972−3980.
(24) Full, J.; Daniel, C.; González, L. *Phys. Chem. Chem. Phys.* **2003**, *5*, 87−96.
(25) Tully, J. C. *J. Chem. Phys.* **1990**, *93*, 1061−1071.
(26) (a) Doltsinis, N. L.; Marx, D. *J. Theory Comput. Chem.* **2002**, *01*, 319−349. (b) González, L.; Marquetand, P.; Richter, M.; González-Vázquez, J.; Sola, I. In *Ultrafast Phenomena in Molecular Sciences*; de Nalda, R., Bañares, L., Eds.; Springer Series in Chemical Physics 107; Springer International Publishing: Cham, Switzerland, 2014; pp 145−170.
(27) Barbatti, M. *WIREs Comput. Mol. Sci.* **2011**, *1*, 620−633.
(28) Moret, M.-E.; Tavernelli, I.; Chergui, M.; Rothlisberger, U. *Chem.—Eur. J.* **2010**, *16*, 5889−5894.
(29) Tavernelli, I.; Curchod, B. F.; Rothlisberger, U. *Chem. Phys.* **2011**, *391*, 101−109.
(30) Pierloot, K. *Int. J. Quantum Chem.* **2011**, *111*, 3291−3301.
(31) González, L.; Escudero, D.; Serrano-Andrés, L. *ChemPhysChem* **2012**, *13*, 28−51.
(32) Jaworska, M. *Inorg. Chem. Commun.* **2006**, *9*, 284−289.
(33) Schenk, G.; Pau, M. Y. M.; Solomon, E. I. *J. Am. Chem. Soc.* **2004**, *126*, 505−515.
(34) Radoń, M.; Broclawik, E.; Pierloot, K. *J. Phys. Chem. B* **2010**, *114*, 1518−1528.
(35) Lahiri, G. K.; Kaim, W. *Dalton Trans.* **2010**, *39*, 4471−4478.
(36) Rose, M. J.; Mascharak, P. K. *Coord. Chem. Rev.* **2008**, *252*, 2093−2114.
(37) Roos, B. O.; Taylor, P. R.; Siegbahn, P. E. *Chem. Phys.* **1980**, *48*, 157−173.
(38) Andersson, K.; Malmqvist, P. A.; Roos, B. O.; Sadlej, A. J.; Wolinski, K. *J. Phys. Chem.* **1990**, *94*, 5483−5488.
(39) Kurtikyan, T. S.; Hayrapetyan, V. A.; Martirosyan, G. G.; Ghazaryan, R. K.; Iretskii, A. V.; Zhao, H.; Pierloot, K.; Ford, P. C. *Chem. Commun.* **2012**, *48*, 12088−12090.
(40) Radoń, M.; Pierloot, K. *J. Phys. Chem. A* **2008**, *112*, 11824−11832.
(41) Daniel, C. *Coord. Chem. Rev.* **2003**, *238−239*, 143−166.
(42) Pierloot, K. *Mol. Phys.* **2003**, *101*, 2083−2094.
(43) Gagliardi, L. In *Reviews in Computational Chemistry*; Lipkowitz, K. B., Cundari, T. R., Eds.; John Wiley & Sons, Inc.: New York, 2007; pp 249−284.
(44) (a) Pedersen, T.; Aquilante, F.; Lindh, R. *Theor. Chem. Acc.* **2009**, *124*, 1−10. (b) Aquilante, F.; Pedersen, T. B.; Lindh, R.; Roos, B. O.; Sánchez de Merás, A.; Koch, H. *J. Chem. Phys.* **2008**, *129*, 024113. (c) Aquilante, F.; Malmqvist, P.-A.; Pedersen, T. B.; Ghosh, A.; Roos, B. O. *J. Chem. Theory Comput.* **2008**, *4*, 694−702.
(45) Delcey, M.; Freitag, L.; Pedersen, T. B.; Aquilante, F.; Lindh, R.; González, L. *J. Chem. Phys.* **2014**, Accepted.
(46) (a) Brahim, H.; Daniel, C.; Rahmouni, A. *Int. J. Quantum Chem.* **2012**, *112*, 2085−2097. (b) Baková, R.; Chergui, M.; Daniel, C.; Vlček, A., Jr.; Záliš, S. *Coord. Chem. Rev.* **2011**, *255*, 975−989. (c) Vallet, V.; Strich, A.; Daniel, C. *Chem. Phys.* **2005**, *311*, 13−18. (d) Kayanuma, M.; Daniel, C.; Köppel, H.; Gindensperger, E. *Coord. Chem. Rev.* **2011**, 255−2703. (e) Heydová, R.; Gindensperger, E.; Romano, R.; Sýkora, J.; Vlček, A.; Záliš, S.; Daniel, C. *J. Phys. Chem. A* **2012**, *116*, 11319−11329.
(47) Marian, C. M. *WIREs Comput. Mol. Sci.* **2012**, *2*, 187−203.
(48) (a) Bhasikuttan, A. C.; Suzuki, M.; Nakashima, S.; Okada, T. *J. Am. Chem. Soc.* **2002**, *124*, 8398−8405. (b) Bhasikuttan, A. C.; Okada, T. *J. Phys. Chem. B* **2004**, *108*, 12629−12632. (c) McCusker, J. K. *Acc. Chem. Res.* **2003**, *36*, 876−887. (d) Cannizzo, A.; van Mourik, F.; Gawelda, W.; Zgrablic, G.; Bressler, C.; Chergui, M. *Angew. Chem., Int. Ed.* **2006**, *118*, 3246−3248. (e) Bräm, O.; Messina, F.; El-Zohry, A. M.; Cannizzo, A.; Chergui, M. *Chem. Phys.* **2012**, *393*, 51−57. (f) Gawelda, W.; Cannizzo, A.; Pham, V.-T.; van Mourik, F.; Bressler, C.; Chergui, M. *J. Am. Chem. Soc.* **2007**, *129*, 8199−8206. (g) Gawelda, W.; Pham, V.-T.; Benfatto, M.; Zaushitsyn, Y.; Kaiser, M.; Grolimund, D.; Johnson, S. L.; Abela, R.; Hauser, A.; Bressler, C.; Chergui, M. *Phys. Rev. Lett.* **2007**, *98*, 057401. (h) Bressler, C.; Milne, C.; Pham, V.-T.; ElNahhas, A.; Veen, R. M. v. d.; Gawelda, W.; Johnson, S.; Beaud, P.; Grolimund, D.; Kaiser, M.; Borca, C. N.; Ingold, G.; Abela, R.; Chergui, M. *Science* **2009**, *323*, 489−492. (i) Consani, C.; Prémont-Schwarz, M.; El Nahhas, A.; Bressler, C.; van Mourik, F.; Cannizzo, A.; Chergui, M. *Angew. Chem., Int. Ed.* **2009**, *48*, 7184−7187. (j) Cannizzo, A.; Milne, C.; Consani, C.; Gawelda, W.; Bressler, C.; van Mourik, F.; Chergui, M. *Coord. Chem. Rev.* **2010**, *254*, 2677−2686. (k) Bräm, O.; Messina, F.; Baranoff, E.; Cannizzo, A.; Nazeeruddin, M. K.; Chergui, M. *J. Phys. Chem. C* **2013**, *117*, 15958−15966. (l) Cannizzo, A.; Blanco-Rodríguez, A. M.; El Nahhas, A.; Šebera, J.; Záliš, S.; Vlček, A., Jr.; Chergui, M. *J. Am. Chem. Soc.* **2008**, *130*, 8967−8974. (m) Juban, E. A.; McCusker, J. K. *J. Am. Chem. Soc.* **2005**, *127*, 6857−6865. (n) Hedley, G. J.; Ruseckas, A.; Samuel, I. D.W. *J. Phys. Chem. A* **2009**, *113*, 2−4. (o) Burdzinski, G. T.; Ramnauth, R.; Chisholm, M. H.; Gustafson, T. L. *J. Am. Chem. Soc.* **2006**, *128*, 6776−6777. (p) Iwakura, I.; Kobayashi, T.; Yabushita, A. *Inorg. Chem.* **2009**, *48*, 3523−3528.
(49) Colvin, M. T.; Smeigh, A. L.; Giacobbe, E. M.; Conron, S. M. M.; Ricks, A. B.; Wasielewski, M. R. *J. Phys. Chem. A* **2011**, *115*, 7538−7549.
(50) (a) Full, J.; González, L.; Daniel, C. *J. Phys. Chem. A* **2001**, *105*, 184−189. (b) González, L.; Daniel, C. *J. Comput. Chem.* **2006**, *27*, 1781−1786. (c) Ambrosek, D.; Villaume, S.; Daniel, C.; González, L. *J.*

Phys. Chem. A **2007**, *111*, 4737−4742. (d) Gindensperger, E.; Köppel, H.; Daniel, C. *Chem. Commun.* **2010**, *46*, 8225. (e) Costa, P. J.; Calhorda, M. J.; Villaume, S.; Daniel, C. *New J. Chem.* **2008**, *32*, 1904.
(51) Perdew, J. P. *Phys. Rev. B* **1986**, *33*, 8822−8824.
(52) Becke, A. D. *J. Chem. Phys.* **1993**, *98*, 5648−5652.
(53) Vahtras, O.; Almlöf, J.; Feyereisen, M. W. *Chem. Phys. Lett.* **1993**, *213*, 514−518.
(54) Eichkorn, K.; Treutler, O.; Öhm, H.; Häser, M.; Ahlrichs, R. *Chem. Phys. Lett.* **1995**, *242*, 652−660.
(55) Sierka, M.; Hogekamp, A.; Ahlrichs, R. *J. Chem. Phys.* **2003**, *118*, 9136−9148.
(56) Schäfer, A.; Horn, H.; Ahlrichs, R. *J. Chem. Phys.* **1992**, *97*, 2571−2577.
(57) Weigend, F.; Ahlrichs, R. *Phys. Chem. Chem. Phys.* **2005**, *7*, 3297−3305.
(58) Andrae, D.; Häußermann, U.; Dolg, M.; Stoll, H.; Preuß, H. *Theor. Chim. Acta* **1990**, *77*, 123−141.
(59) Eichkorn, K.; Weigend, F.; Treutler, O.; Ahlrichs, R. *Theor. Chem. Acc.* **1997**, *97*, 119−124.
(60) Klamt, A.; Schüürmann, G. *J. Chem. Soc., Perkin Trans. 2* **1993**, 799−805.
(61) TURBOMOLE V6.5, 2013, a development of University of Karlsruhe and Forschungszentrum Karlsruhe GmbH, 1989−2007, TURBOMOLE GmbH, since 2007; available from http://www.turbomole.com.
(62) Aquilante, F.; de Vico, L.; Ferré, N.; Ghigo, G.; Malmqvist, P.-Å.; Neogrády, P.; Pedersen, T. B.; Pitoňák, M.; Reiher, M.; Roos, B. O.; Serrano-Andrés, L.; Urban, M.; Veryazov, V.; Lindh, R. *J. Comput. Chem.* **2010**, *31*, 224−247.
(63) Roos, B. O.; Lindh, R.; Malmqvist, P.-A.; Veryazov, V.; Widmark, P.-O. *J. Phys. Chem. A* **2005**, *109*, 6575−6579.
(64) Finley, J.; Malmqvist, P. A.; Roos, B. O.; Serrano-Andrés, L. *Chem. Phys. Lett.* **1998**, *288*, 299−306.
(65) Roos, B. O.; Andersson, K. *Chem. Phys. Lett.* **1995**, *245*, 215−223.
(66) Cossi, M.; Rega, N.; Scalmani, G.; Barone, V. *J. Comput. Chem.* **2003**, *24*, 669−681.
(67) Malmqvist, P. A.; Roos, B. O.; Schimmelpfennig, B. *Chem. Phys. Lett.* **2002**, *357*, 230−240.
(68) Barbatti, M.; Aquino, A. J. A.; Lischka, H. *Phys. Chem. Chem. Phys.* **2010**, *12*, 4959.
(69) Verlet, L. *Phys. Rev.* **1967**, *159*, 98−103.
(70) Richter, M.; Marquetand, P.; González-Vázquez, J.; Sola, I.; González, L. *J. Chem. Theory Comput.* **2011**, *7*, 1253−1258.
(71) (a) Richter, M.; Marquetand, P.; González-Vázquez, J.; Sola, I.; González, L. *J. Phys. Chem. Lett.* **2012**, *3*, 3090−3095. (b) Mai, S.; Marquetand, P.; Richter, M.; González- Vázquez, J.; González, L. *ChemPhysChem* **2013**, *14*, 2920−2931. (c) Mai, S.; Marquetand, P.; González, L. *J. Chem. Phys.* **2014**, accepted.
(72) Tapavicza, E.; Tavernelli, I.; Rothlisberger, U. *Phys. Rev. Lett.* **2007**, *98*, 023001.
(73) Tavernelli, I.; Curchod, B. F. E.; Rothlisberger, U. *J. Chem. Phys.* **2009**, *131*, 196101.
(74) Tavernelli, I.; Curchod, B. F. E.; Laktionov, A.; Rothlisberger, U. *J. Chem. Phys.* **2010**, *133*, 194104.
(75) (a) Casida, M. E.; Natarajan, B.; Deutsch, T. In *Fundamentals of Time-Dependent Density Functional Theory*; Marques, M. A. L.; Maitra, N. T.; Nogueira, F. M. S.; Gross, E. K. U.; Rubio, A., Eds.; Lecture Notes in Physics 837; Springer: Berlin, 2012; pp 279−299. (b) Huix-Rotllant, M.; Filatov, M.; Gozem, S.; Schapiro, I.; Olivucci, M.; Ferré, N. *J. Chem. Theory Comput.* **2013**, *9*, 3917−3932. (c) Cordova, F.; Doriol, L. J.; Ipatov, A.; Casida, M. E.; Filippi, C.; Vela, A. *J. Chem. Phys.* **2007**, *127*, 164111.
(76) (a) Tapavicza, E.; Tavernelli, I.; Rothlisberger, U.; Filippi, C.; Casida, M. E. *J. Chem. Phys.* **2008**, *129*, 124108. (b) Tapavicza, E.; Meyer, A. M.; Furche, F. *Phys. Chem. Chem. Phys.* **2011**, *13*, 20986−20998. (c) Tapavicza, E.; Bellchambers, G. D.; Vincent, J. C.; Furche, F. *Phys. Chem. Chem. Phys.* **2013**, *15*, 18336−18348. (d) Curchod, B. F. E.; Rothlisberger, U.; Tavernelli, I. *ChemPhysChem* **2013**, *14*, 1314−1340.
(77) Lower, S. K.; El-Sayed, M. A. *Chem. Rev.* **1966**, *66*, 199−241.
(78) Manaa, M. R.; Yarkony, D. R. *J. Chem. Phys.* **1991**, *95*, 1808−1816.
(79) Merchán, M.; Serrano-Andrés, L.; Robb, M. A.; Blancafort, L. *J. Am. Chem. Soc.* **2005**, *127*, 1820−1825.
(80) Escudero, D.; Happ, B.; Winter, A.; Hager, M. D.; Schubert, U. S.; González, L. *Chem. Asian J.* **2012**, *7*, 667−671.
(81) Hammes-Schiffer, S.; Tully, J. C. *J. Chem. Phys.* **1994**, *101*, 4657.
(82) Pittner, J.; Lischka, H.; Barbatti, M. *Chem. Phys.* **2009**, *356*, 147−152.
(83) Barbatti, M.; Ruckenbauer, M.; Plasser, F.; Pittner, J.; Granucci, G.; Persico, M.; Lischka, H. *WIREs Comput. Mol. Sci.* **2014**, *4*, 26−33.
(84) Enemark, J. H.; Feltham, R. D. *J. Am. Chem. Soc.* **1974**, *96*, 5002−5004.
(85) (a) Tong, G. S. M.; Wong, E. L.-M.; Che, C.-M. *Chem.—Eur. J.* **2008**, *14*, 5495−5506. (b) Carreón-Macedo, J.-L.; Harvey, J. N. *J. Am. Chem. Soc.* **2004**, *126*, 5789−5797. (c) Kuta, J.; Patchkovskii, S.; Zgierski, M. Z.; Kozlowski, P. M. *J. Comput. Chem.* **2006**, *27*, 1429−1437. (d) Lodowski, P.; Jaworska, M.; Andruniów, T.; Kumar, M.; Kozlowski, P. M. *J. Phys. Chem. B* **2009**, *113*, 6898−6909. (e) Jaworska, M.; Lodowski, P.; Andruniów, T.; Kozlowski, P. M. *J. Phys. Chem. B* **2007**, *111*, 2419−2422. (f) DeBeer George, S.; Petrenko, T.; Neese, F. *J. Phys. Chem. A* **2008**, *112*, 12936−12943. (g) Goossen, L. J.; Koley, D.; Hermann, H. L.; Thiel, W. *J. Am. Chem. Soc.* **2005**, *127*, 11102−11114.
(86) Ziegler, T.; Seth, M.; Krykunov, M.; Autschbach, J.; Wang, F. *THEOCHEM* **2009**, *914*, 106−109.
(87) Casida, M. E.; Gutierrez, F.; Guan, J.; Gadea, F.-X.; Salahub, D.; Daudey, J.-P. *J. Chem. Phys.* **2000**, *113*, 7062−7071.
(88) Giesbertz, K.; Baerends, E. *Chem. Phys. Lett.* **2008**, *461*, 338−342.